

Appendix B

B.1 Fibre manufacturing and fibre doping

B.1.1 Optical fibre manufacturing

Optical fibre manufacturing can be split into three steps: preform forming, drawing and coating. The preform has a similar structure and index profile as the wanted fibre and can be used beforehand to examine the expected fibre quality, for example, whether the fibre possesses core ellipticity, by using a preform analyser (see Figure C.5, Appendix C). There are several methods for manufacturing the preform but they all use some kind of vapour deposition technology, e.g. modified chemical vapour deposition (MCVD) or outside vapour deposition (OVD). In MCVD, the chemical vapour deposition which builds up the core and cladding flows into a rotating silica tube which is heated from outside, and after deposition the tube is collapsed into a rod [225]. OVD, developed by Corning Glass Works, uses a rotating starting rod and the core and cladding is deposited from outside onto the rod [226]. The MCVD and OVD methods are of interest in this thesis since all the fibres we used for measuring birefringence and DGD are made by using one of the two methods. It is interesting to note that fibres manufactured using the MCVD technique suffer from higher ellipticity compared to OVD [66], [91]. The fibre ellipticity using MCVD originates mainly from the noncircularity in the silica tube which gets impressed in the fibre core and cladding after collapsing the tube.

B.1.2 Fibre doping of core and cladding

The refractive index difference between core and cladding, which is necessary for guiding the light, can be achieved by doping either the core and/or the cladding. Figure B.1 shows some examples of dopants which can be used. For low loss high reliability fibres, different dopant combinations are possible. With MCVD, as used at BT Labs, Ipswich, UK, a matched cladding technique is used for the step index fibre for manufacturing reasons. The core is doped with ~3 mol% GeO₂ and the cladding with ~2 mol% P₂O₅ and ~1 mol% F. In general, the doping level for manufacturing the fibre is more of a trial and error technique [91]. For DS fibres, BT Labs uses a rectangular profile (see Figure C.5, Appendix C) where the inner layer of the core is doped with about 8 mol% GeO₂ and the cladding with P₂O₅ and F, as for the step index fibre. For OVD, as developed and used by Corning, only the core is doped with GeO₂ [105]. For small doping concentrations, a simple linear equation for the refractive index

difference as a function of the doping level with GeO₂ can be derived, by using Sellmeiers equation [71], as

$$\Delta \approx 0.106 \cdot x \quad (B.1)$$

where x is the GeO₂ concentration in mol%.

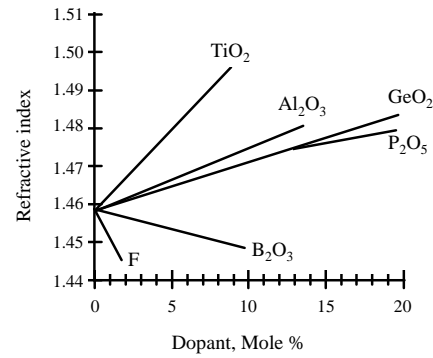


Figure B.1 Refractive index for common dopants of SiO₂ (From[66])

B.1.3 Birefringence, DPD and DGD due to shape and stress birefringence

To compute the thermal stress birefringence due to core ellipticity from doping the cladding with P₂O₅ and F, the matched cladding technique is assumed so that Δ can be taken as constant. The thermal expansion coefficients for P₂O₅ and GeO₂ have been considered in the following simulations, as given in Table 3.1.

Figure B.2 shows the simulation result for the shape, $\delta\beta_G$, and the corresponding thermal stress birefringence, $\delta\beta_S$, with and without Phosphor in the cladding as a function of the V value for S-SMF. The shape birefringence is essentially independent of the doping (Equation 3.27) and is mainly determined by the core ellipticity which has been taken as 1%.

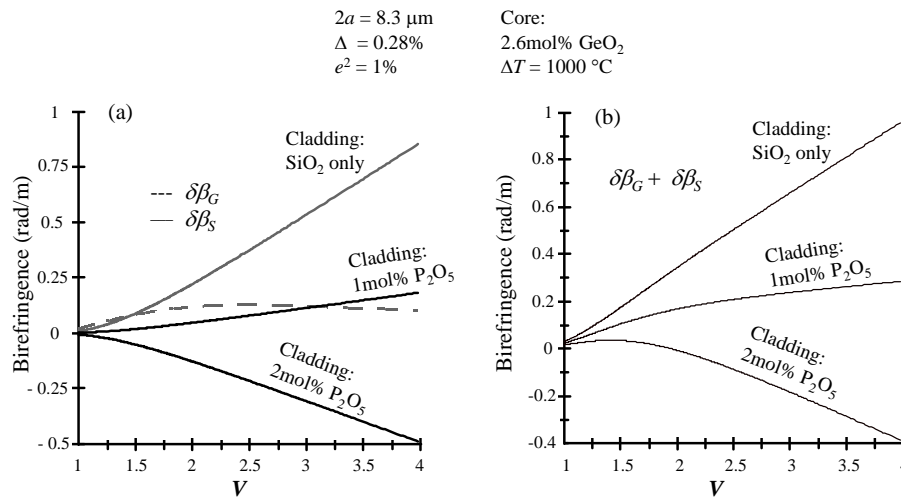


Figure B.2 Simulation of $\delta\beta_G$ and $\delta\beta_S$ as a function of the V value with and without Phosphor doping in the cladding, with $C(\lambda)$ and $n(\lambda)$.

The use of P₂O₅ in the cladding, as used by BT Labs (DEDF 2), makes the thermal expansion coefficient difference in Equation (3.29) (stress birefringence) smaller, and as can be seen in

Figure B.2, at some doping level inverts the sign so that $\delta\beta_G$ and $\delta\beta_S$ are in opposition, i.e. their fast axes are orthogonal. The two birefringence effects can thus partially cancel each other and fibre with low birefringence and low PMD can result.

In Figure B.3(a), the calculated DGD and DPD are plotted for the birefringence of the S-SMF in Figure B.2(b) for 1% ellipticity. The solid line in Figure B.3(a) corresponds to the DGD and the dashed line in Figure B.3(a) shows the DPD. It can be seen that for 1 mol% P_2O_5 in the cladding, the DGD due to the thermal stress contribution is minimised, compared to the case without doping in the cladding, as expected from the reduced thermal stress birefringence in Figure B.2(a). For larger doping of the core, a sign inversion occurs, and the DGD due to the thermal stress birefringence starts again to be the dominant contribution to the total DGD.

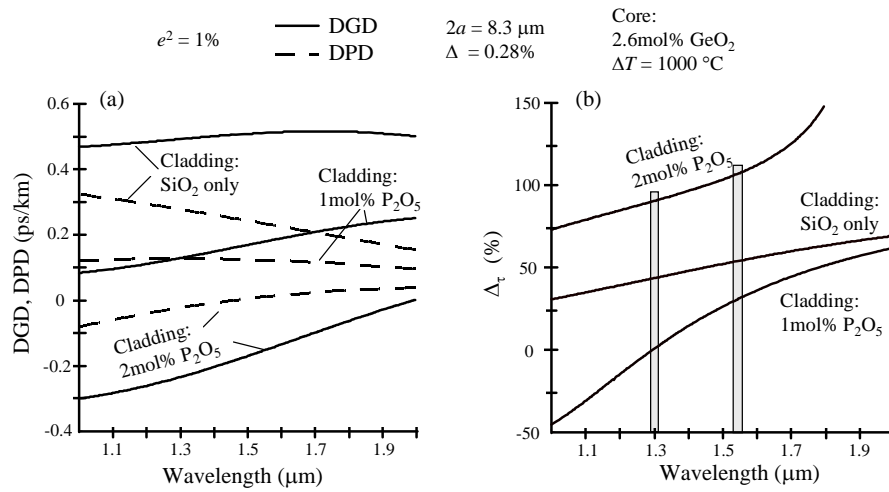


Figure B.3 S-SMF (a) DGD and DPD due to $\delta\beta_G + \delta\beta_S$ with and without Phosphor in the cladding (b) relative difference in DGD and DPD.

The relative difference Δ_r of the DGD and DPD is plotted in Figure B.3(b) as a function of wavelength. It can now be seen that even for fixed values of core diameter, a , and relative refractive index difference, Δ , the minimum and maximum difference in the DGD and DPD can be between 25% and 100% at 1.55 μm depending on the Phosphor level in the cladding. This difference in the DGD and DPD would of course make it more difficult, in addition to variation of the fibre parameters a and Δ (see Figure 3.15), to accurately calculate from the measured birefringence at a single wavelength the DGD for such a fibre (Chapter 7, POTDR).

B.2 PSP - DGD equation in rotating reference frame

B.2.1 The DGD vector equation for twisted fibres

The magnitude of the DGD vector $\vec{\Omega}$ can be evaluated directly in the rotating frame, as shown in Subsection 5.2.3. In the rotating frame, it can be shown that the dispersion vector is composed of two components, one is parallel to $\delta\hat{\beta} = [\delta\beta_L \ 0 \ -(2-g)\gamma]^T / \delta\beta$ and grows linearly with length, whilst the other is orthogonal to $\delta\hat{\beta}$, of constant magnitude with length, and follows a circular motion in the plane orthogonal to $\delta\hat{\beta}$. The rotation matrix in the rotating frame is given by Equation 5.30 as

$$\mathbf{R}(\delta\vec{\beta}l) = \mathbf{I} + \sin(\delta\beta l)\mathbf{B} + (1 - \cos(\delta\beta l))\mathbf{B}^2 \quad (\text{B.2})$$

where \mathbf{B} is the skew-symmetric matrix defined in Equation (5.27). The derivative of $\mathbf{R}(\delta\vec{\beta}l)$ with respect to optical frequency is given by

$$\begin{aligned} \mathbf{R}' &= \cos(\delta\beta l)l\delta\beta'\mathbf{B} + \sin(\delta\beta l)\mathbf{B}' + \sin(\delta\beta l)l\delta\beta'\mathbf{B}^2 + (1 - \cos(\delta\beta l))(\mathbf{B}'\mathbf{B} + \mathbf{B}\mathbf{B}') \\ &= (\cos(\delta\beta l)\mathbf{B} + \sin(\delta\beta l)\mathbf{B}^2)\delta\beta'l + (\sin(\delta\beta l)\mathbf{B}' + (1 - \cos(\delta\beta l))(\mathbf{B}'\mathbf{B} + \mathbf{B}\mathbf{B}')) \end{aligned} \quad (\text{B.3})$$

Multiplying the length growing part of \mathbf{R}' with the transpose of the rotation gives the polarisation dispersion matrix $\mathbf{\Omega}$ in the rotating reference frame (Equation 5.38)

$$\mathbf{\Omega} = \mathbf{R}'\mathbf{R}^T = (\cos(\delta\beta l)\mathbf{B} + \sin(\delta\beta l)\mathbf{B}^2)l\delta\beta'(\mathbf{I} - \sin(\delta\beta l)\mathbf{B} + (1 - \cos(\delta\beta l))\mathbf{B}^2) \quad (\text{B.4})$$

where the property $\mathbf{B}^T = -\mathbf{B}$ has been used. Using $-\mathbf{B} = \mathbf{B}^3$ (Equation 5.10) Equation (B.4) can be re-written as

$$\mathbf{\Omega} = \mathbf{R}'\mathbf{R}^T = \delta\beta'\mathbf{B}l \quad (\text{B.5})$$

or in vector notation

$$\vec{\Omega} = \delta\beta'\delta\hat{\beta}l \quad (\text{B.6})$$

where the normalised rotation axis of the skew-symmetric matrix \mathbf{B} is given by $\delta\hat{\beta} = [\delta\beta_L \ 0 \ -(2-g)\gamma]^T / \delta\beta$. Equation (B.6) shows that the DGD vector is growing linearly with length parallel to $\delta\hat{\beta}$ as given in Equation (5.44).

B.2.2 The small oscillating term

Multiplication of the oscillating term of the dispersion matrix Equation (B.3) with the transpose of the rotation matrix, Equation (B.2), gives

$$\Omega^* = \left(\sin(\delta\beta l) \mathbf{B}' + (1 - \cos(\delta\beta l)) (\mathbf{B}'\mathbf{B} + \mathbf{B}\mathbf{B}') \right) \left(\mathbf{I} - \sin(\delta\beta l) \mathbf{B} + (1 - \cos(\delta\beta l)) \mathbf{B}^2 \right) \quad (\text{B.7})$$

using $\mathbf{B}\mathbf{B}'\mathbf{B} = 0$ and $-\mathbf{B} = \mathbf{B}^3$ Equation (B.7) can be re-written as

$$\begin{aligned} \Omega^* &= \sin(\delta\beta l) \mathbf{B}' + (1 - \cos(\delta\beta l)) \mathbf{B}\mathbf{B}' - \sin^2(\delta\beta l) \mathbf{B}'\mathbf{B} + (1 - \cos(\delta\beta l)) \cos(\delta\beta l) \mathbf{B}'\mathbf{B} \\ &= \sin(\delta\beta l) \mathbf{B}' + (1 - \cos(\delta\beta l)) \mathbf{B}\mathbf{B}' - (1 - \cos(\delta\beta l)) \mathbf{B}'\mathbf{B} \end{aligned} \quad (\text{B.8})$$

substituting into Equation (B.8) $\mathbf{B}'\bar{\mathbf{s}} = \delta\hat{\beta}' \times \bar{\mathbf{s}}$, $\mathbf{B}\mathbf{B}'\bar{\mathbf{s}} = \delta\hat{\beta}' \delta\hat{\beta}'^T \bar{\mathbf{s}}$ and $\mathbf{B}'\mathbf{B}\bar{\mathbf{s}} = \delta\hat{\beta} \delta\hat{\beta}'^T \bar{\mathbf{s}}$

$$\begin{aligned} \Omega\bar{\mathbf{s}} &= \sin(\delta\beta l) \delta\hat{\beta}' \times \bar{\mathbf{s}} + (1 - \cos(\delta\beta l)) \delta\hat{\beta}' \delta\hat{\beta}'^T \bar{\mathbf{s}} - (1 - \cos(\delta\beta l)) \delta\hat{\beta} \delta\hat{\beta}'^T \bar{\mathbf{s}} \\ &= \sin(\delta\beta l) \delta\hat{\beta}' \times \bar{\mathbf{s}} + (1 - \cos(\delta\beta l)) \left(\delta\hat{\beta}' \delta\hat{\beta}'^T - \delta\hat{\beta} \delta\hat{\beta}'^T \right) \bar{\mathbf{s}} \end{aligned} \quad (\text{B.9})$$

The last term in Equation (B.9) can be re-written in vector index notation; using the

Kronecker delta δ_{ij} which is defined as $\delta_{i,j} = \begin{cases} 1 & \text{if } i = j \\ 0 & \text{otherwise} \end{cases}$ and the permutation symbol ε_{ijk}

defined in Equation (5.9)

$$\begin{aligned} \left(\delta\hat{\beta}' \delta\hat{\beta}'^T - \delta\hat{\beta} \delta\hat{\beta}'^T \right)_{ij} &= \delta\hat{\beta}'_i \delta\hat{\beta}'_j - \delta\hat{\beta}_i \delta\hat{\beta}'_j = (\delta_{ii} \delta_{jm} - \delta_{im} \delta_{ji}) \delta\hat{\beta}'_m \delta\hat{\beta}'_l \\ &= \varepsilon_{kij} \varepsilon_{klm} \delta\hat{\beta}'_l \delta\hat{\beta}'_m = \varepsilon_{ijk} \left(\delta\hat{\beta} \times \delta\hat{\beta}' \right)_k \end{aligned} \quad (\text{B.10})$$

where $\varepsilon_{ijk} \left(\delta\hat{\beta} \times \delta\hat{\beta}' \right)_k$ is the searched skew-symmetric matrix which can be written in vector

form as $\left(\delta\hat{\beta} \times \delta\hat{\beta}' \right)_{ij}$. The oscillating term of the dispersion matrix can be written in vector

form as given in Equation (5.44) as

$$\bar{\Omega}^* = \sin(\delta\beta l) \frac{d(\delta\hat{\beta})}{d\omega} + (1 - \cos(\delta\beta l)) \left(\delta\hat{\beta} \times \frac{d(\delta\hat{\beta})}{d\omega} \right) \quad (\text{B.11})$$

B.2.3 The orthogonality of the small oscillating terms to $\hat{\delta\beta}$

Proof that $\hat{\delta\beta}'$ is orthogonal to $\hat{\delta\beta}$:

(i) $\hat{\delta\beta}$ is a unit vector and $\hat{\delta\beta} \cdot \hat{\delta\beta} = 1$.

$$(ii) \frac{d(\hat{\delta\beta} \cdot \hat{\delta\beta})}{d\omega} = \frac{d(\hat{\delta\beta})}{d\omega} \cdot \hat{\delta\beta} + \hat{\delta\beta} \cdot \frac{d(\hat{\delta\beta})}{d\omega} = 2 \frac{d(\hat{\delta\beta})}{d\omega} \cdot \hat{\delta\beta}$$

(iii) Because $\frac{d(1)}{d\omega} = 0$ (ii) only holds if $\hat{\delta\beta}'$ is orthogonal to $\hat{\delta\beta}$

B.3 Spun fibres with sinusoidal spin and uniform elastic twist

B.3.1 DGD of spun fibres with sinusoidal spin as a function of elastic twist at different lengths

In Figure B.4, the length dependence of the DGD for spun fibre with sinusoidal spin as a function of external applied twist has been investigated. The initial birefringence of DSF Spun 4 which, for an effective spin of $\tilde{\gamma}_{rms} \approx 4.4$ turns/m, showed some fluctuation in its DGD with external twist (see Figure 6.17), has been chosen for the simulation to show that these peak values grow linearly with fibre length. The fibre parameters for the simulated fibre in Figure B.4 are:

$$\delta\beta_L = 2.55 \text{ rad/m} \rightarrow \text{DGD}(\gamma=0) \approx 2.1 \text{ ps/km}$$

$$\Lambda_\gamma = 2 \text{ m and } A_\gamma = 2 \times 2\pi \text{ radians}$$

The calculated DGD values have been normalised to the used simulation lengths to show directly the linear relationship between the simulation lengths at 16, 50, 100 and 200 metres. It can be seen for the different lengths in Figure B.4 that the peak DGD values can be taken as growing linearly with fibre length, justifying the normalisation of the DGD to the fibre length, as shown in Section 6.3 for the spun fibre.

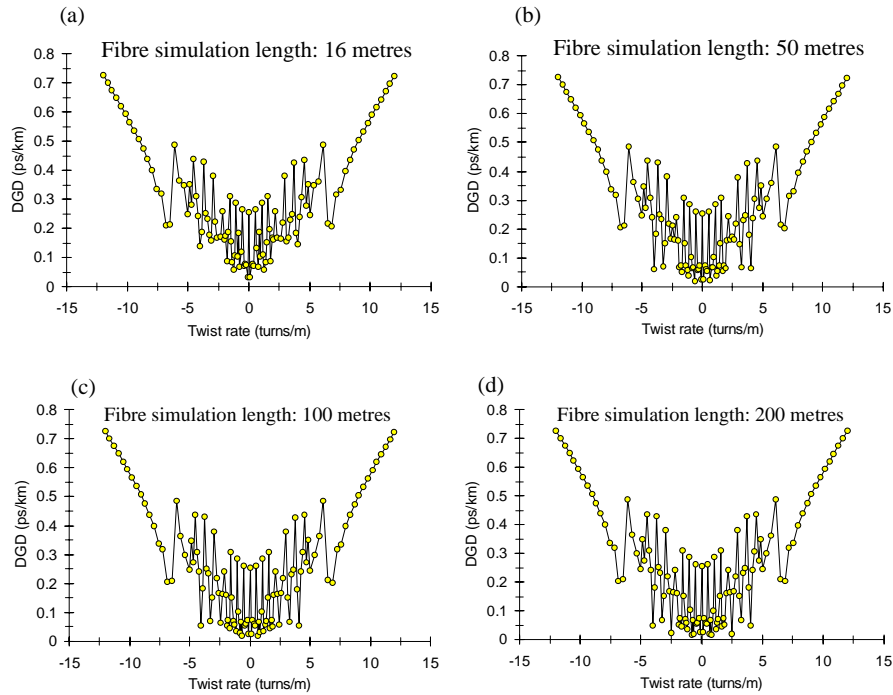


Figure B.4 Numerical calculation of DGD versus external applied twist for DSF Spun 4 for different fibre lengths. In (a) for 16 m, (b) for 50 m, (c) for 100 m and in (d) for 200 m.

Figure B.5 (a) and (b) shows the DGD versus external twist for an effective spin rate of $\tilde{\gamma}_{rms} = 8.9$ turns/m for DSF Spun 4 and 3 respectively. The same effective spin has been used in Figure 6.18(a) for DSF Spun 4 and in Figure 6.20(a) for DSF 3, but using different spin amplitude A_γ , and spin periods Λ_γ , showing roughly the same effective DGD reduction for both fibres because of the same effective spin used.

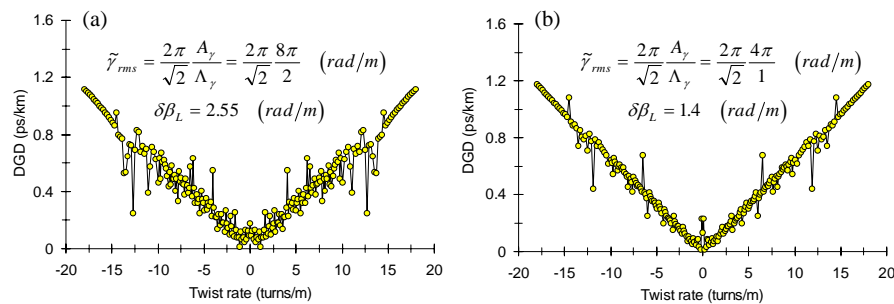


Figure B.5 Numerical calculation of DGD versus external applied twist for $\tilde{\gamma}_{rms} \approx 8.9$ turns/m In (a) for DSF Spun 4 and in (b) for DSF Spun 3.

B.4 Reported PMD values from networks across Europe

Table B.1 lists reported PMD values from different network operators across Europe. It can be seen that in some countries, like Germany or Denmark, older cables may limit future upgrades to 10 Gbit/s TDM (e.g. for $\text{PMD} = 2 \text{ ps}/\sqrt{\text{km}}$ the maximum length is $\sim 20 \text{ km}$, see Figure 6.24).

Fibre type	Fibre length (km)	PMD ($\text{ps}/\sqrt{\text{km}}$)	Operator & Reference
Old cables installed 1984 & 1989	18 - 38.7	Max. 2.7 Min. 0.2 Mean. 0.8	Deutsche Telekom AG [189]
New cables	21.2 - 125.6	Max. 0.15 Min. 0.05 Mean. 0.1	
~ Fifty cables S-SMF	5 - 70	Max. 0.809 Min. 0.014 Mean. 0.112	Telia Swedish Telecom [191]
DSF	168	~ 1	Telecom Italia [14]
S-SMF	74	~ 0.17	Telecom Italia [190]
S-SMF	74	~ 0.06	
Thirteen fibres S-SMFs	43 - 133	Max. 1.64 Min. 0.33 Mean. 0.73	Tele Denmark [187]
S-SMF	19 - 39	Max. 1.9 Min. 0.063 Mean. 0.8	Swiss Telecom PTT [187]
DSF	73	1	

Table B.1 Review of PMD measurement results in installed systems.

B.5 More POTDR simulation and measurement results

B.5.1 POTDR results on untwisted fibres using DFB and Fabry-Perot laser

Figure B.6 shows the backscattered SOP evolution on the Poincaré sphere, measured with the single-channel POTDR using three different configurations: (a) a DFB with no fibre polariser in the output path of the POTDR, (b) a DFB with fibre polariser at the output path and (c) with a Fabry-Perot laser and a fibre polariser at the output path. The measurements have been made on S-SMF 2 at about zero twist position, showing a SOP evolution close to a circle for all three.

The average DOP (Figure B.6) of the backscattered SOPs is the highest for the DFB laser with fibre polariser at the output path. For the DFB laser without a fibre polariser at the output the average DOP is just slightly lower. This is most probably due to the small change of the output SOP during the measurement time as shown in Figure 7.11(b). For the Fabry-Perot laser with fibre polariser, the average DOP is the lowest, due to the presence of one isolator after the fibre polariser.

Figure B.6 also shows the error angle ε calculated from two repeated POTDR measurement results on S-SMF 2. It can now be clearly seen for the DFB laser that the fibre polariser at the output, path reduces the error in the measured backscattered SOP. The error in the SOP with polariser is now even lower than that for the four-channel POTDR, shown in Figure 7.26(b). For the Fabry-Perot laser, the error in the measured SOP is about the same as that for the DFB laser without polariser.

From the discussion above, we can conclude that the error in the backscattered SOP measurement can be reduced by using a polariser at the output path, which insures that the launched pulses into the fibre under test are well polarised and are stable over measurement time. On the other hand, there is some additional loss due to the fibre polariser.

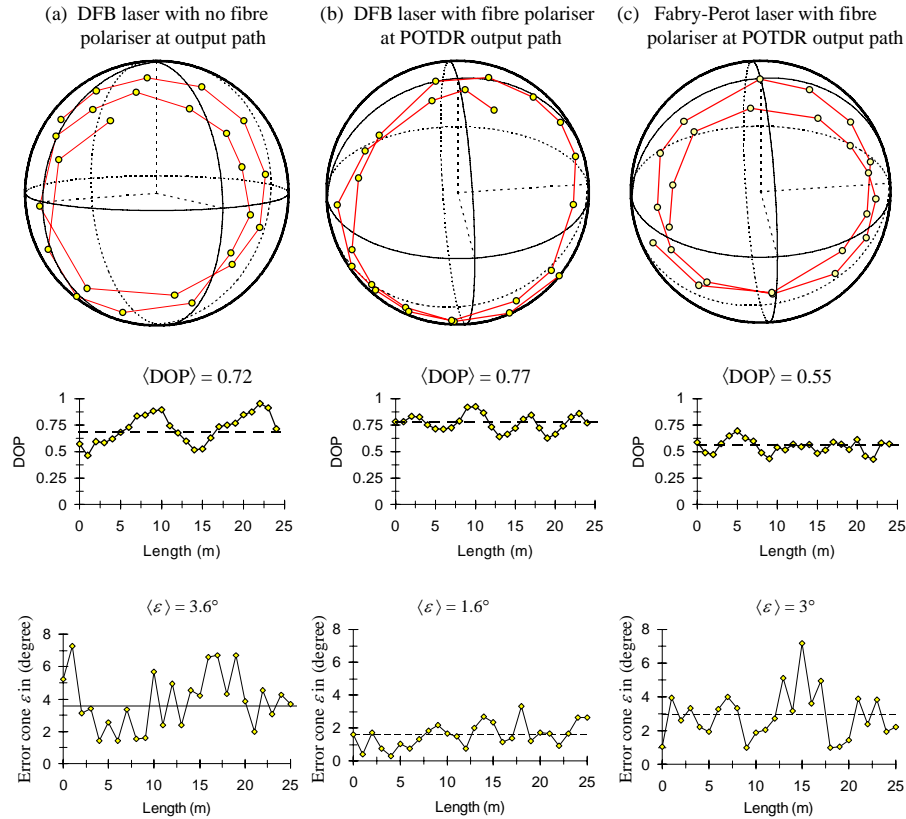


Figure B.6 Measured SOP evolution, DOP and error angle ε along S-SMF 2 at about zero twist using the single-channel POTDR. In (a) with a DFB laser and no fibre polariser at the POTDR output path, (b) with a DFB laser and fibre polariser at the POTDR output path and (c) with a Fabry-Perot laser and fibre polariser at the POTDR output path.

B.5.2 Error in analysing optics for single-channel POTDR

For the single-channel POTDR, the largest error angle ε in the analysing optics is due to the error in the $\lambda/4$ waveplate which is less than $\pm 1.5\%$ at $\lambda = 1.55 \mu\text{m}$ (see Subsection 4.4). Figure B.7 shows the computed error angle ε as a function of the SOP for an error in the $\lambda/4$ retardation waveplate of $\pm 1.5\%$ and assuming zero noise. This showed that the average error over all the possible SOPs is $\langle \varepsilon \rangle = 0.4^\circ$. The total error in the SOP and measured DOP is a complicated function of the true SOP and analysing optics, hence the asymmetry of the shape of the DOP_M , Figure B.7(b), arising from the particularly chosen polariser and $\lambda/4$ plate

positions. However, the mean error remains approximately the same for a given error in the $\lambda/4$ plate¹.

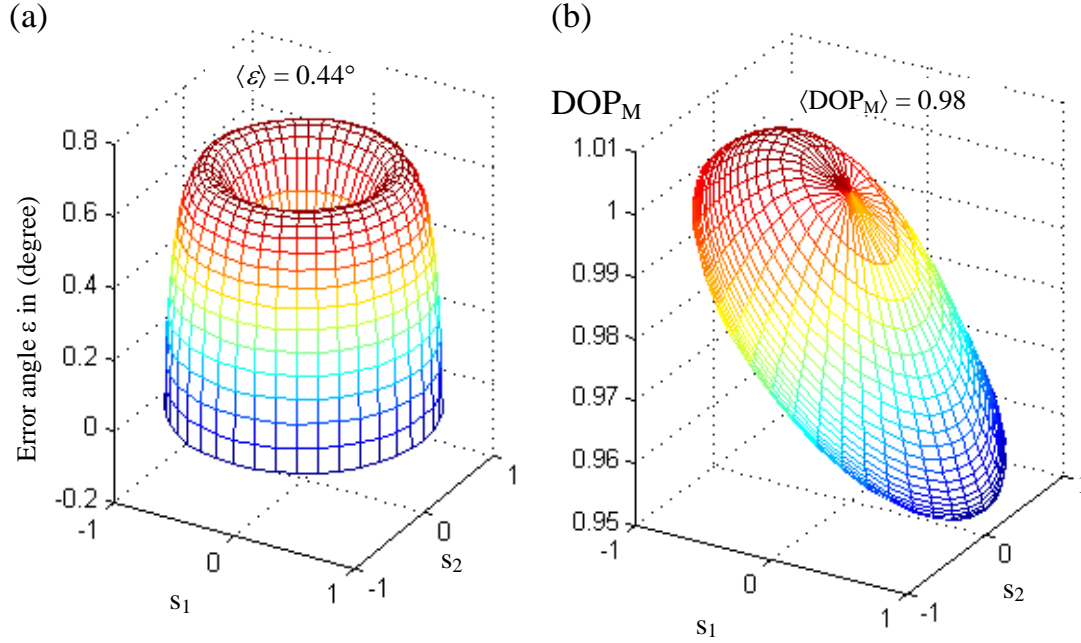


Figure B.7 Error in measured SOP for one channel polarimeter for fully polarised light with $\Delta d_3 = \lambda/4 \times 1.5\%$ and no noise ($s_3 = \sqrt{1 - s_1^2 - s_2^2}$). In (a) error angle ϵ and in (b) measured DOP.

B.5.2 Backscattered SOP evolution for increasing $\gamma/\delta\beta_L$.

Finding the best fit for the backscattered SOP evolution along a fibre at the presence of twist, measured with a POTDR, is not a simple task. This is because there are basically three parameters, $\delta\beta_L$, γ , and the input SOP, which determine the three dimensional shape of the SOP evolution on the Poincaré sphere. However, the periodicity of the backscattered SOP evolution is independent of the input SOP and is given in Equation 7.9 and 7.8 for the cases with and without twist. The shape of the SOP evolution on the Poincaré sphere does not change for a fixed input SOP and for $\gamma/\delta\beta_L = \text{constant}$. For the analysis of the measured POTDR traces in Chapter 7, we have mainly chosen backscatter traces which show a figure of eight shape on the Poincaré sphere, which made it simpler to find the correct input SOP.

¹ For Figure B.7, the four rotational positions of the $\lambda/4$ plate have been taken as 0° , 40° , 80° and 120° and the polariser as fixed at 0° .

This, in fact, is a very convenient way for analysing the SOP traces, but requires adjustment of the input SOP until the figure of eight appears in the backscatter trace. In general, an automated procedure which could analyse the POTDR traces independent of the input SOP, as mentioned in Subsection 8.2.2 is desirable.

Figure B.8 shows the backscattered SOP evolution for four different input SOPs and for increasing $\gamma/\delta\beta_L$. In (a) the figure of eight shaped SOP evolution is apparent when the input SOP excites both PEMs equally (with a linear input SOP). This trace is preferred for POTDR analysis, because it shows a great circle at zero twist and the recognisable figure of eight, and whose enclosed area continuously decreases with increasing $\gamma/\delta\beta_L$. In (b), although both PEMs are excited equally, the trace is asymmetrical due to the elliptical input SOP. In (c) and (d), exciting one PEM only and exciting the PEMs unequally respectively, leads to further variations in the backscattered SOP evolution.

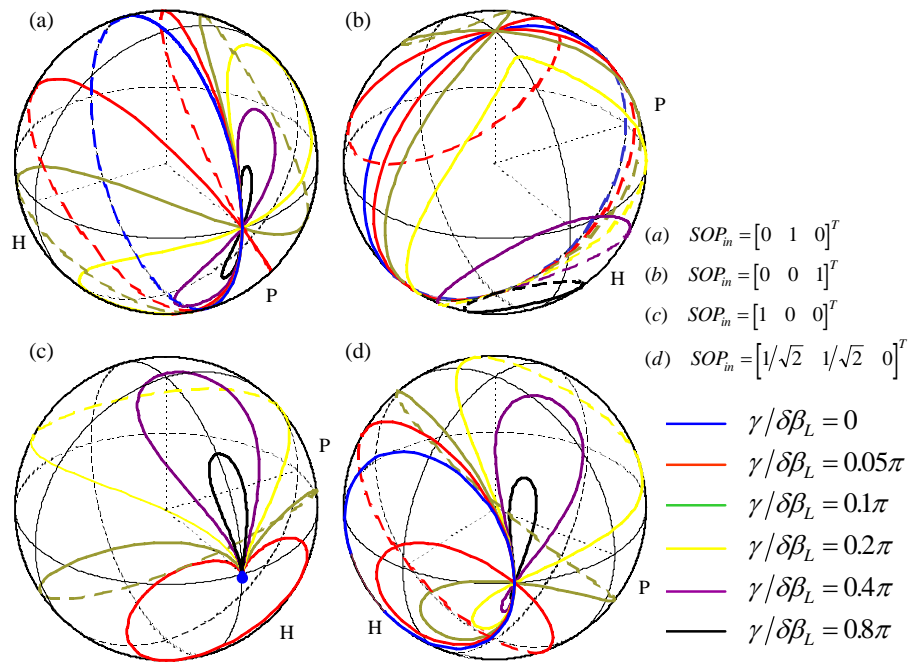


Figure B.8 The dependence of the backscattered SOP evolution on the ratio $\gamma/\delta\beta_L$ and the input SOP.

Figure B.9 shows the measured backscattered SOP evolution on S-SMF 3 with the single-channel POTDR, for two different input SOPs as a function of increasing $\gamma/\delta\beta_L$. For both input SOPs, the backscattered SOP evolution shows a figure of eight shape whose enclosed area decreases with increasing $\gamma/\delta\beta_L$ as expected from Figure B.8(a). In finding the linear and twist induced circular birefringence, we could now use Equation 7.12 to find the best fit, as

used throughout Chapter 7. However, a more elegant method would be as indicated in Figure B.9 to estimate from the opening of the figure of eight or the size of the SOP trace, the angle α , which in Equation 7.10 determines the shape of the SOP evolution. If α and the periodicity of the SOP evolution L are known, the linear and twist induced circular birefringence can be directly obtained from Equations 7.9 and 7.10.

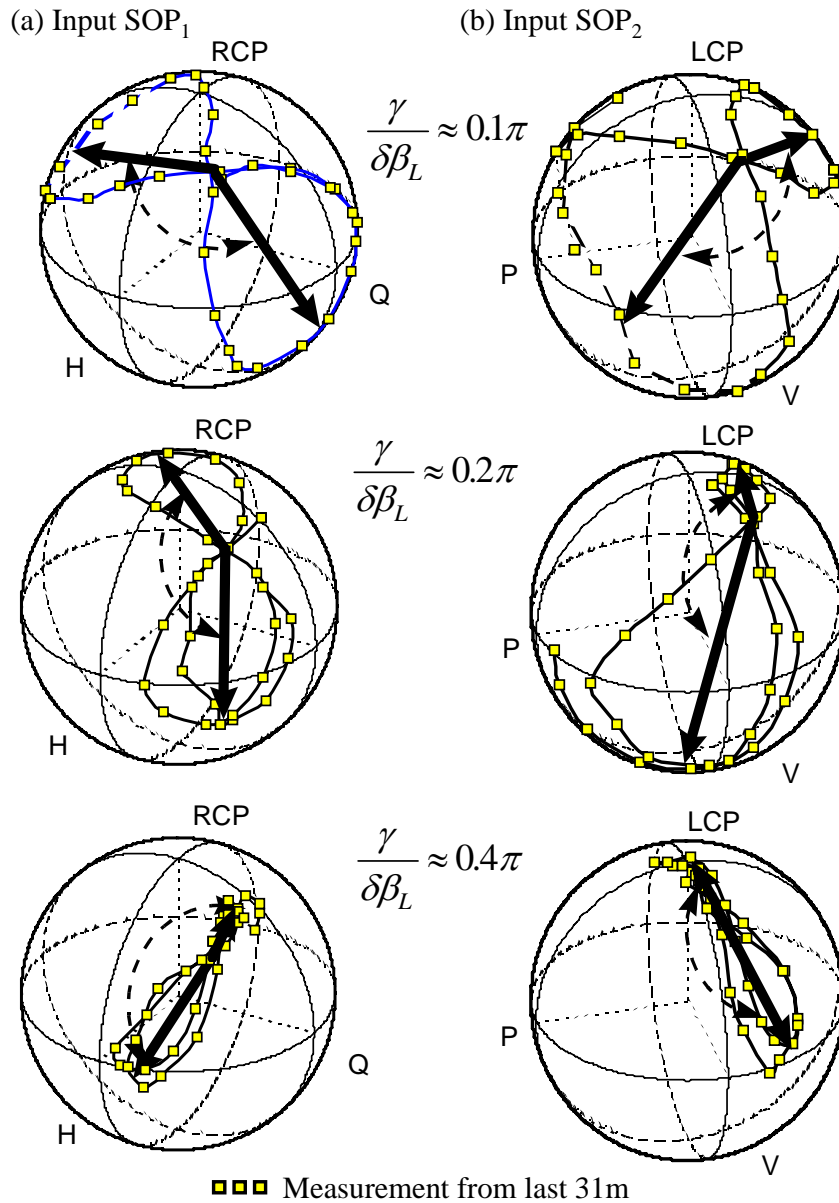


Figure B.9 The progression of the backscattered SOP evolution for increasing $\gamma/\delta\beta_L$, for two different input SOPs as indicated in (a) and (b).